Geophysical Journal International

Geophys. J. Int. (2023) **233,** 1018–1035
Advance Access publication 2022 December 12
GJI Seismology

https://doi.org/10.1093/gji/ggac493

Seismic source mapping by surface wave time reversal: application to the great 2004 Sumatra earthquake

Apsara Sharma Dhakal,[1] Irene Molinari [2] and Lapo Boschi [1,2,3]

[1] *Dipartimento di Geoscienze, Universitá degli Studi di,* 35131 *Padova, Italy. E-mail: apsara.sharmadhakal@studenti.unipd.it*
[2] *Istituto Nazionale di Geofisica e Vulcanologia, Sezione di,* 40128 *Bologna, Italy*
[3] *Institut des Sciences de la Terre Paris, Sorbonne Université, CNRS-INSU, ISTeP UMR* 7193, *F-*75005 *Paris, France*

Accepted 2022 December 4. Received 2022 November 25; in original form 2022 April 21

SUMMARY

Different approaches to map seismic rupture in space and time often lead to incoherent results for the same event. Building on earlier work by our team, we 'time-reverse' and 'backpropagate' seismic surface wave recordings to study the focusing of the time-reversed field at the seismic source. Currently used source-imaging methods relying on seismic recordings neglect the information carried by surface waves, and mostly focus on the *P*-wave arrival alone. Our new method combines seismic time reversal approach with a surface wave ray-tracing algorithm based on a generalized spherical-harmonic parametrization of surface wave phase velocity, accounting for azimuthal anisotropy. It is applied to surface wave signal filtered within narrow-frequency bands, so that the inherently 3-D problem of simulating surface wave propagation is separated into a suite of 2-D problems, each of relatively limited computational cost. We validate our method through a number of synthetic tests, then apply it to the great 2004 Sumatra–Andaman earthquake, characterized by the extremely large extent of the ruptured fault. Many studies have estimated its rupture characteristics from seismological data (e.g. Lomax, Ni *et al.*, Guilbert *et al.*, Ishii *et al.*, Krüger & Ohrnberger, Jaffe *et al.*) and geodetic data (e.g. Banerjee *et al.*, Catherine *et al.*, Vigny *et al.*, Hashimoto *et al.,* Bletery *et al.*). Applying our technique to recordings from only 89 stations of the Global Seismographic Network (GSN) and bandpass filtering the corresponding surface wave signal around 80-to-120, 50-to-110 and 40-to-90 s, we reproduce the findings of earlier studies, including in particular the northward direction of rupture propagation, its approximate spatial extent and duration, and the locations of the areas where most energy appears to be released.

Key words: Earthquake source observations; Surface waves and free oscillations; Theoretical seismology; Wave propagation.

1 INTRODUCTION

The problem of reconstructing the slip distribution on a seismic fault is notoriously non-unique (Mai *et al.* 2016). Our study is motivated by the idea that non-uniqueness could be reduced by taking into account a section of the seismogram that is usually not included in source inversions: the surface waves. The benefits of harvesting such information, in the context of seismic source inversion, were illustrated in some detail by Boschi *et al.* (2018): the fact that surface waves are dispersive emphasizes the focusing of backpropagated time-reversed signal at the source; their broad frequency range should help constraining source structure at different depth and/or of different scale length; the fact that a narrow-band-filtered surface wave can be approximated as a membrane wave (Tanimoto 1990; Tromp & Dahlen 1993; Peter *et al.* 2007, 2009) results in simpler and less computationally intensive software. We exploit the Rayleigh waves to reconstruct the seismic source by time-reversing and backpropagating (Fink 1999, 2006 Fink *et al.* 2003) filtered vertical-component seismograms from a relatively large number of broad-band stations distributed as uniformly as possible around the globe and along all azimuths from the epicentre. In practice, we conduct wave-propagation simulations where receivers act as virtual sources, emitting the real-world signal that they have recorded, but reversed with respect to time. Time-reversed signals are propagated through a reliable earth model and eventually focus on the real-world source (the earthquake).

The method that we describe and validate here is an extension to the global scale of that of Boschi *et al.* (2018): the flat-earth ray-tracing scheme is replaced with the one of Boschi & Woodhouse (2006) in order to calculate surface wave ray paths on a spherical earth and,

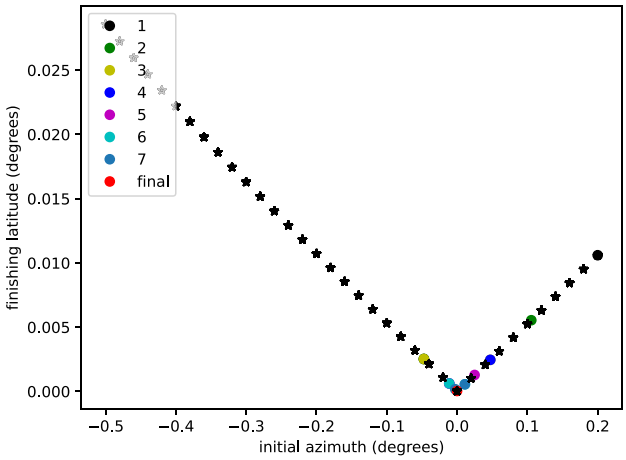

Figure 1. Finishing latitude as a function of the initial azimuth obtained using the golden-section-search method implemented in this study (coloured circles) and the brute-force method of Boschi & Woodhouse (2006). Our new approach reduces computation time by about one order of magnitude. Finishing latitude = 0 corresponds to convergence to the correct ray path.

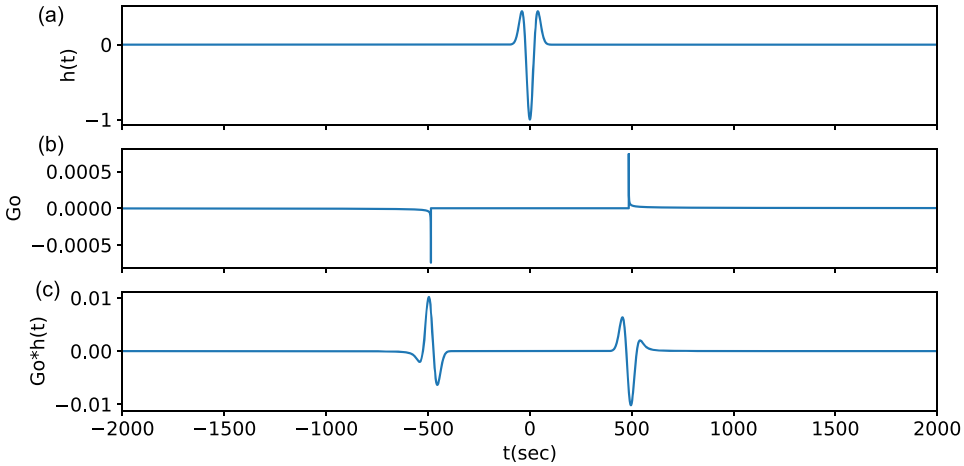

Figure 2. (a) Source time function (100 s ricker wavelet), (b) Green's function with interstation distance 2000 km and wave speed 4.12 km s^{-1} and (c) convolution of (a) and (b).

importantly, allows to account not only for isotropic phase velocity heterogeneity, but also for laterally varying azimuthal anisotropy of surface waves. Compared to other declinations of so-called time-reversal and/or backpropagation of seismic waves, our source-imaging method is restricted to surface wave data, which can be approximated as membrane waves and modelled both via ray-tracing or numerical simulations. Conversely, backprojection as described, for example, by Ishii *et al.* (2005) have systematically been restricted to body wave (typically *P*-wave) traveltimes, with the sole exception of a surface wave study by Roten *et al.* (2012); time-reversal seismology as implemented by Larmat *et al.* (2006, 2008) relies on the more rigorous, but computationally much more demanding, numerical 3-D modelling of the entire seismic waveform. In the following we describe our method, validate it via application to global-scale synthetic data, and apply it to a set of broad-band recordings of the 2004 December 26, Sumatra–Andaman Earthquake. Sumatra is one of the most studied earthquakes in history, with a well-documented rupture of long duration and large spatial extent. Our results are compared with those obtained from high-frequency body wave (Lomax 2005; Ni *et al.* 2005), tsunami data (Lay *et al.* 2005), geodetic data (Jaffe et al. 2006; Catherine et al. 2005; Vigny et al. 2005; Hashimoto et al. 2006) and array analysis (Guilbert *et al.* 2005; Ishii *et al.* 2005; Krüger & Ohrnberger 2005; Yao *et al.* 2011) . We find that the robust features of the Sumatran rupture, confirmed by most of the mentioned studies, are reproduced by our method as well, and we consider this to be an important confirmation of its validity.

2 THEORY AND METHODS

2.1 Surface wave modelling via ray tracing

Surface waves propagate along the Earth's outer surface, and they involve the oscillation of the earth's crust and top of the upper mantle. Surface wave are dispersive meaning that different periods are sensitive to Earth structure at different depths (typically maximum at a depth

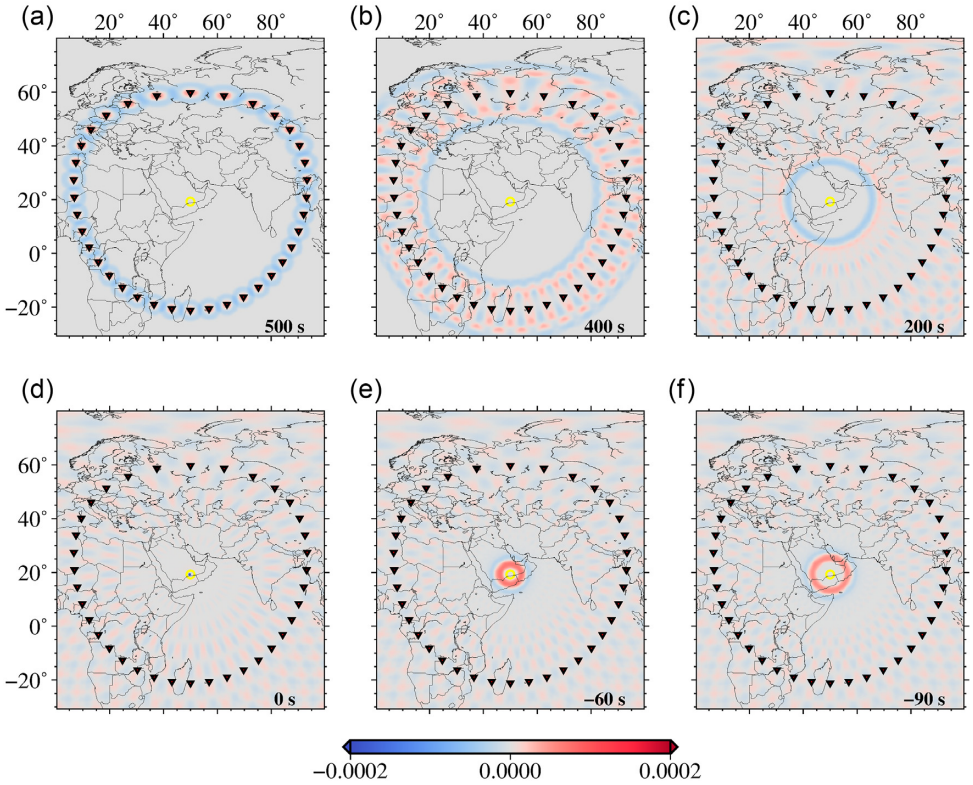

Figure 3. Snapshots of time-reversal simulation where 100 s surface waves are modelled in a heterogeneous, isotropic phase velocity model and backpropagated in the same model. In this synthetic experiment, stations (inverted triangles) are distributed along a 'circle' of radius 4500 km, centered at the source location (yellow circle). Snapshot (d) corresponds to focusing of the time-reversed wavefield onto the location of the source. The time $t = 0$s corresponds to the origin time; positive time indicates the time just before focusing onto the source location.

roughly equal to half a wavelength) and their velocity depend on the mechanical properties of the earth at the depth range of interest. A practical consequence of surface wave dispersion is that their propagation can be studied separately for a set of narrow-frequency bands (e.g. Ekström *et al.* 1997), or surface wave 'modes', each with its own laterally varying phase velocity and, consequently, propagation path along the earth surface. Starting with the early study of Tanimoto & Anderson (1985), surface waves have been known to be azimuthally anisotropic, that is, their velocity depends locally on their direction of propagation. Smith & Dahlen (1973, 1975) show that a relative perturbation in phase velocity c, with respect to a reference value c_0, can be written

$$\frac{\delta c(\theta,\phi,\zeta)}{c_o} = \varepsilon_0(\theta,\phi) + \varepsilon_1(\theta,\phi)\cos(2\zeta) + \varepsilon_2(\theta,\phi)\sin(2\zeta) + \varepsilon_3(\theta,\phi)\cos(4\zeta) + \varepsilon_4(\theta,\phi)\sin(4\zeta), \tag{1}$$

where θ, ϕ denote latitude and longitude, respectively, along the earth's surface, ζ is the azimuth of propagation, and the four functions ε_1, ε_2, etc. are all required to describe propagation in the presence of azimuthal anisotropy ($\varepsilon_0(\theta,\phi)$ coincides with isotropic velocity heterogeneity). At each location θ, ϕ, an independent set of values for ε_0, ε_1, etc., is associated to each surface wave frequency, that is, to each surface wave mode. These azimuthal terms ε_i are functions of frequency because of surface wave dispersion, and depend in a known way on the 21 anisotropic elastic parameters of the medium through which the waves is propagating. Our method allows for surface wave azimuthal anisotropy, which we parametrize according to the generalized-spherical-harmonic scheme described by Trampert & Woodhouse (2003) and Boschi & Woodhouse (2006). Boschi & Woodhouse (2006) discuss the effectiveness of this parametrization for tracing surface wave ray paths, in particular in the presence of azimuthal anisotropy, which makes simpler isotropic velocity parametrization schemes inadequate. Surface wave rays are traced according to the ray-tracing equations given, for example, by Larson *et al.* (1998),

$$\frac{d\theta}{d\phi} = -\frac{\sin(\theta)(\tan(\zeta) + \partial_\zeta \ln c)}{1 - \tan(\zeta)\partial_\zeta \ln c}, \tag{2}$$

$$\frac{d\zeta}{d\phi} = \frac{\sin(\theta)\partial_\theta \ln c + \tan(\zeta)\partial_\phi \ln c - \cos(\theta)}{1 - \tan(\zeta)\partial_\zeta \ln c}, \tag{3}$$

The differential eqs (2) and (3) describe how the latitude and azimuth change as functions of longitude along the ray path, and they are most effectively integrated in a reference frame where source and receiver are located on the equator. We solve them following Boschi &

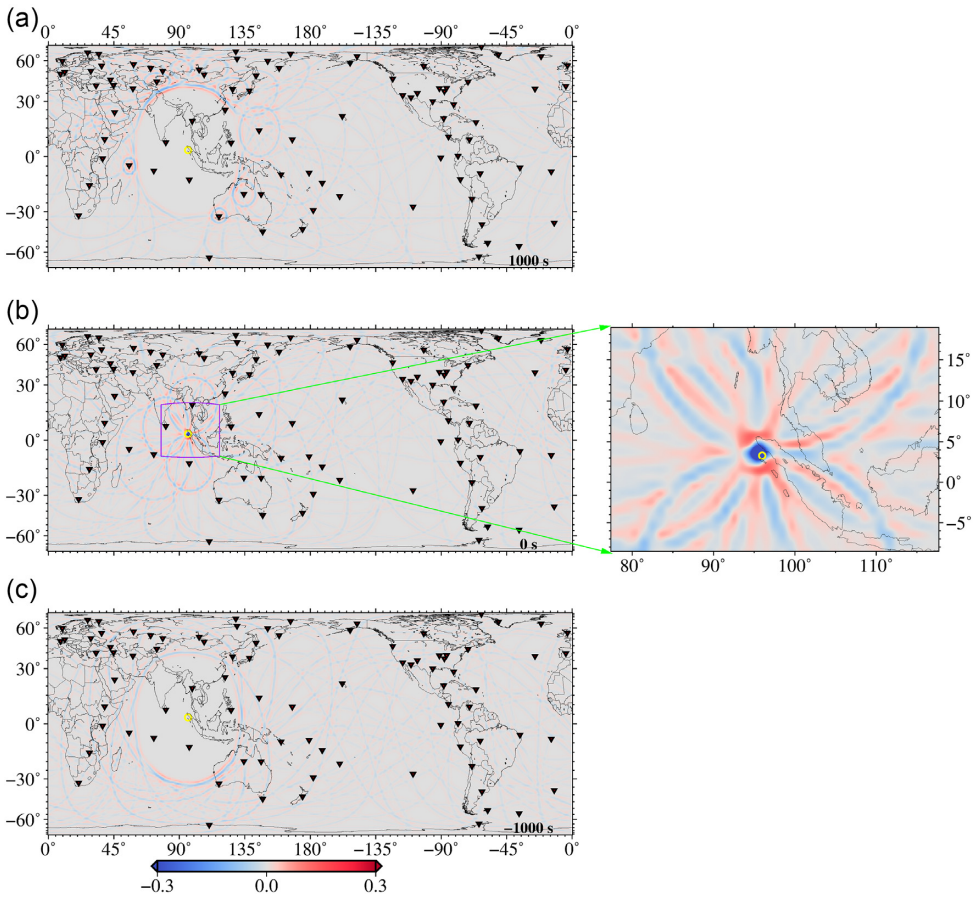

Figure 4. Similar to Fig. 3, snapshots of time-reversal simulation where 100 s surface waves are modelled in a heterogeneous, isotropic phase velocity model and backpropagated in the same model. Negative time show non-physical signal that continues to propagate after focusing. Panel on the right shows an enlarged detail of the source region from the map in panel (b), that is, the origin time, as indicated by the green lines.

Woodhouse (2006), starting with the values of θ and ϕ that correspond to one of the endpoints of the ray, making a guess for the initial azimuth, and integrating numerically until the other endpoint is reached (in practice, a point along the ray path is found when the distance from the ray endpoint is smaller than a certain threshold), or an unreasonably large distance is covered. In the former case, the ray has been successfully traced, while in the latter, the integration should be repeated, assigning a different value to the initial azimuth. In mathematical terms, this is an example of applying the 'shooting method' to solve a two-point boundary value problem (e.g. Press *et al.* 1992).

Because seismic/acoustic time reversal is more effective the more recordings are backpropagated, our experiment requires many ray paths to be traced; we accordingly optimized the search for the correct initial azimuth, reducing the number of iterations via the 'golden-section search method' (e.g. Press *et al.* 1992, chap 10), allowing very fast convergence to the correct initial azimuth and ray path. We compared the new ray-tracing method implemented here against that of Boschi & Woodhouse (2006), using both to trace rays between a large set of randomly located sources and receivers. The gain in both computational speed and accuracy is evident. An example is shown in Fig. 1, with source and station located at (42.80°N, 16.70°E) and (43.04°N, 12.66°E) respectively. In this case, the golden-search method achieves convergence after 8 iterations while the 'brute-force approach' of Boschi & Woodhouse (2006) required 36 iterations. A similar improvement is found regardless of source and station locations.

Once the ray path between two points is determined, Rayleigh-wave phase can be calculated as described by Boschi & Woodhouse (2006).

2.2 Surface-wave time reversal

Because of the spatial reciprocity and time invariance of the elastic wave equation, a time-reversed wavefield focuses on its original source. In a medium that is slightly heterogeneous like the earth focusing is achieved, in practice, if the wavefield is recorded at (and backpropagated from) a uniformly distributed set of receivers that cover all azimuths of propagation (e.g. Fink 1999, 2006; Fink *et al.* 2003).

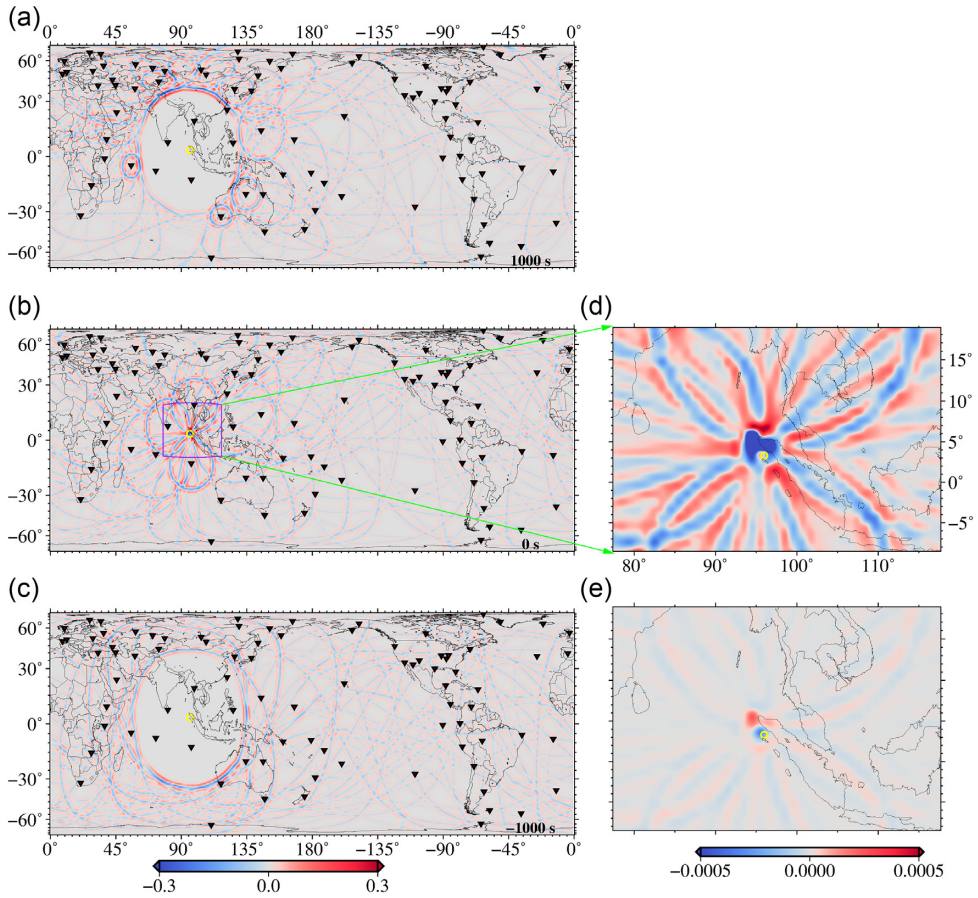

Figure 5. Snapshots of the time-reversal simulation obtained by using synthetic data computed in heterogeneous model and backpropagated through homogeneous model. The times at which the wavefield is shown are same as Fig. 4, and, likewise, the image in panel (d) is a detail of that in panel (b). Panel (e) shows the difference between the time-reversed wavefield displayed here, and that of Fig. 4(b), that is, the error caused by neglecting heterogeneity in phase velocity. The colour scale in panel (e) is different than the one used in all other panels, because the error is very small.

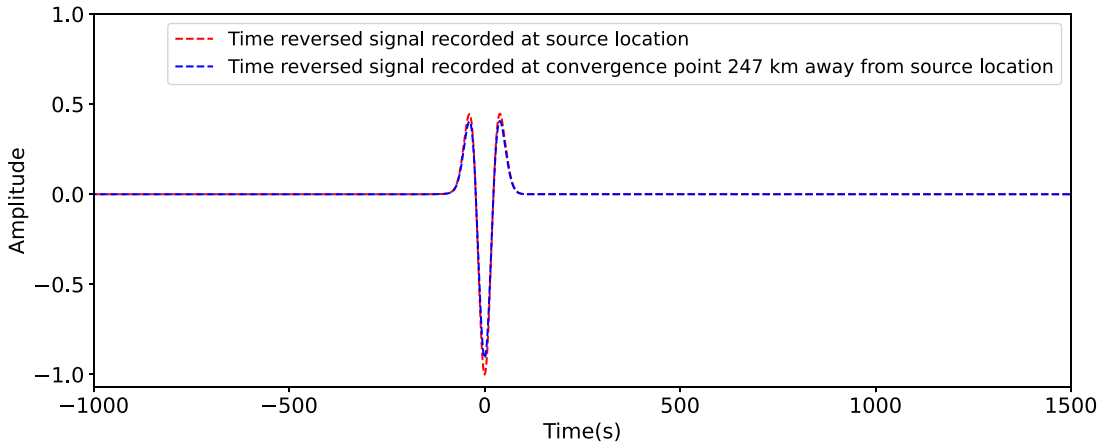

Figure 6. Time-reversed and backpropagated displacement at and near the source location, resulting from the time-reversal simulation of Figs 4 and 5. The red dashed curve is obtained using synthetic data from heterogeneous model and backpropagated through the same heterogeneous model while the blue dashed curve is obtained using synthetic data from heterogeneous model and backpropagated through homogeneous model. At time $t = 0$ s, peaks are not equally sharp.

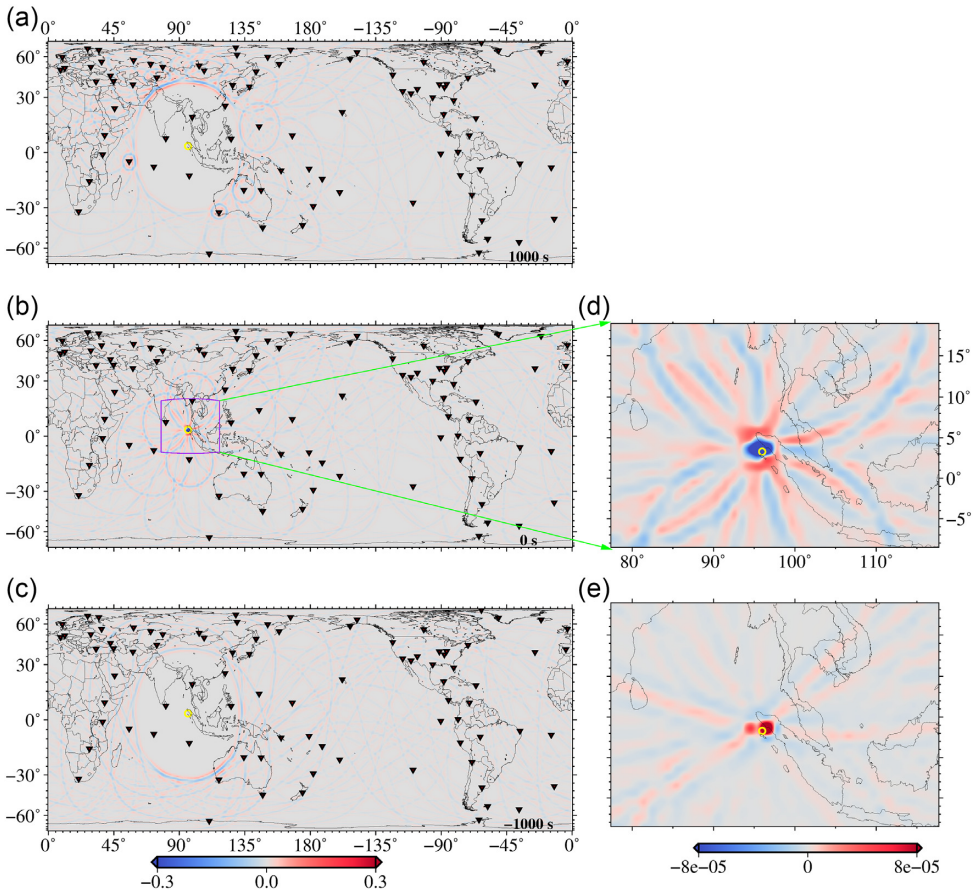

Figure 7. Snapshots of the time-reversal simulation obtained from synthetic data computed in a heterogeneous, anisotropic model and backpropagated through the exact same model. Snapshots were selected at the same times as in Fig. 4. Panel (e) is the zoomed-in plot representing the difference between time-reversed wavefield obtained when anisotropy is accounted for and neglected. The colour scale in panel (e) is different than the one used in all other panels as the error is very small.

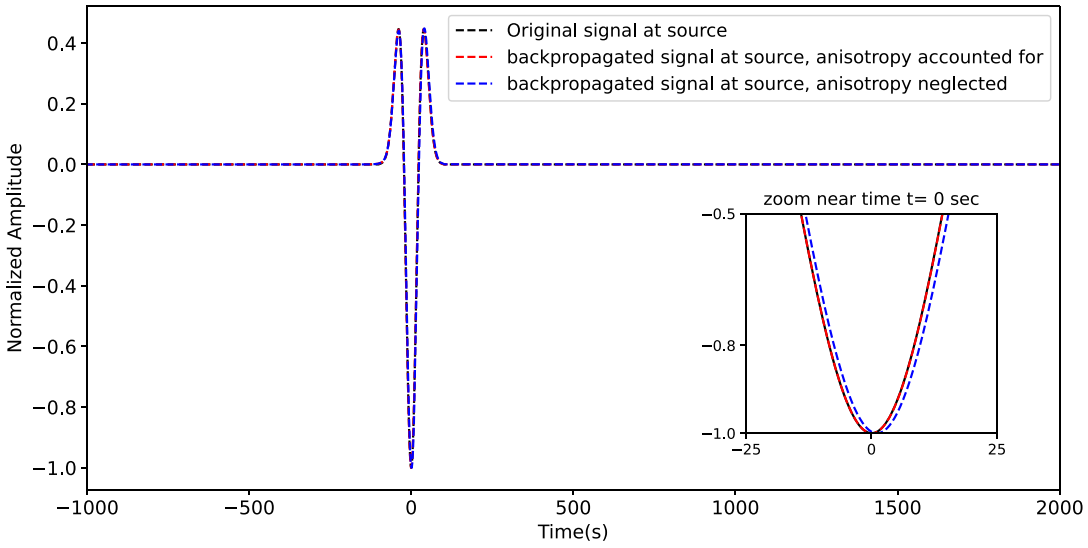

Figure 8. Normalized time-reversed backpropagated displacement at the location of the source, resulting from the time-reversal simulation of Fig. 7. Synthetics were computed in a heterogeneous, anisotropic phase-velocity model and backpropagated in the same heterogeneous model without (blue dashed curve) and with anisotropy (red dashed curve). When anisotropy is accounted for, the source signal is reproduced almost perfectly; neglecting anisotropy results in a discrepancy of the order of 1 s.

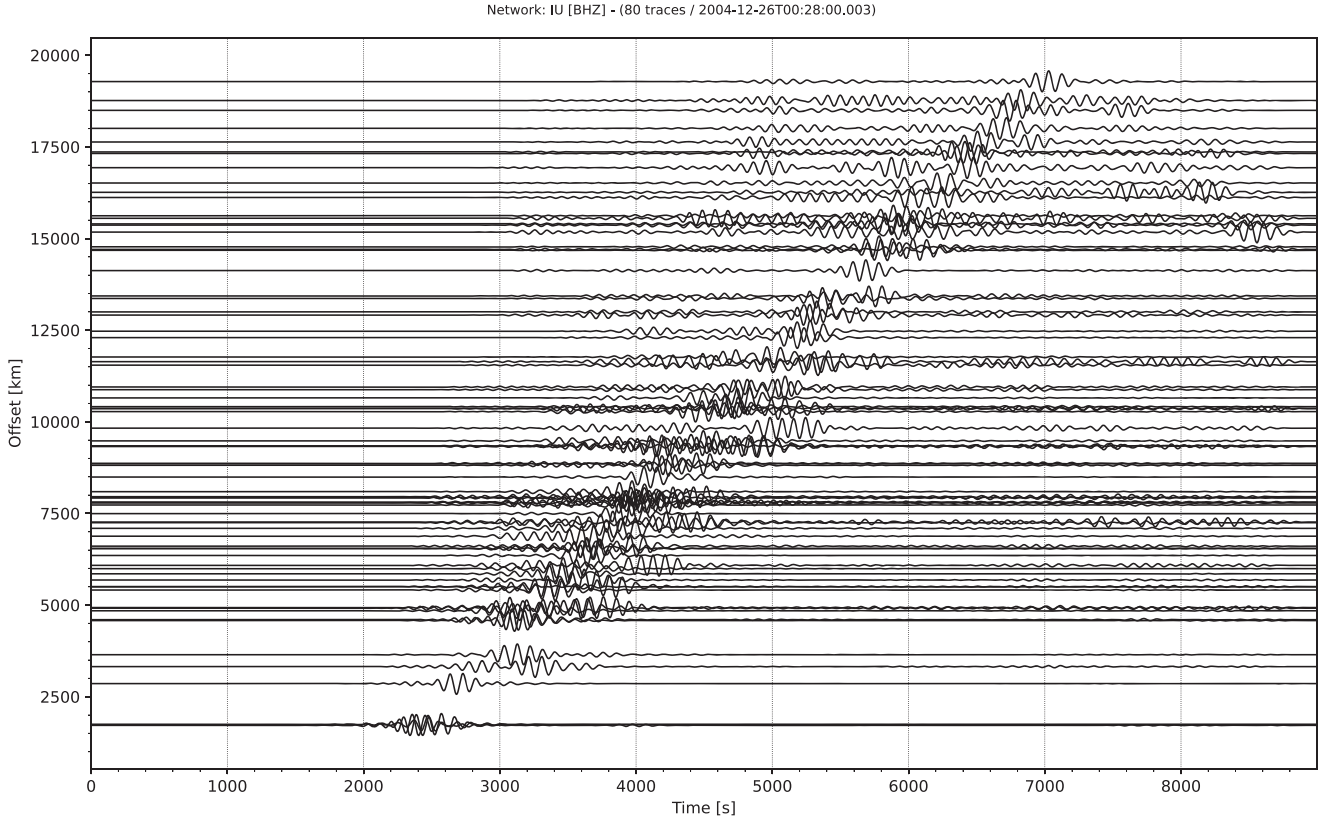

Figure 9. Vertical component recordings of M_w 9.3 Sumatra earthquake from 89 IRIS/USGS GSN, filtered in the period bands 80-to- 120 s.

In seismology, the time-reversal concept can help to reconstruct the location, geometry and mechanics of an earthquake. However, seismic data are very sensitive to heterogeneities in earth structure, and the distribution of seismic stations is not always uniform (in fact, it can be very non-uniform depending on the scale of the problem, and/or the geographic area of study). The effectiveness of seismic time-reversal is accordingly limited by station distribution and errors in the velocity models used to simulate wave (back)propagation. Rietbrock & Scherbaum (1994) made a first attempt at seismic time reversal, but limited to local scale and to the acoustic approximation (compressional waves only). Larmat *et al.* (2006, 2008) time reversed the entire seismic waveform, backpropagating it in a global, heterogeneous earth model via 3-D numerical simulation. The computational cost of such endeavor forced them to low-pass filter the data, studying only the longer wavelength portion of the seismic signal.

Many other authors (Ishii *et al.* 2005; Krüger & Ohrnberger 2005; Lay *et al.* 2005; Merrifield *et al.* 2005; Ni *et al.* 2005; Yao *et al.* 2011) backpropagated only the arrival time of seismic signal, neglecting waveform information; this is usually referred to as backpropagation rather than time reversal, and is usually limited to body waves. Only Roten *et al.* (2012) have tried to backpropagate the arrival times of surface wave modes, but without any advanced modelling of wave propagation, and neglecting the information carried by the waveform (amplitude).

Surface wave backpropagation can be implemented via the membrane-wave approach (Peter *et al.* 2009; Tanimoto 1990), reducing the 3-D momentum equation to 2-D by separating the contribution of each mode and modelling each mode separately, which significantly reduces the computational costs. This simple approach is sufficient to correctly model the phase of individual surface wave modes. Thus, if one considers only the phase, and not the amplitude of surface waves, multiple forms of data analysis (imaging, backpropagation) are possible using the surface wave potentials and associated 2-D scalar equation.

Here, we reduce the problem to two dimensions, similar to Peter *et al.* (2009), but, rather than implementing finite-element simulations to model wave propagation, we trace the rays as in Boschi *et al.* (2018). The equivalence of the two approaches is discussed by Boschi *et al.* (2018).

The theory of surface wave time reversal can be summarized by the frequency-domain eq. (45) of Boschi *et al.* (2018), that reads

$$h^*(\omega)\left[G^*_{2D}(\mathbf{x}_A,\mathbf{x}_B,\omega)-G_{2D}(\mathbf{x}_B,\mathbf{x}_A,\omega)\right]\approx\frac{2i\omega}{c_o}\int_{\partial s}d\mathbf{x}'\left[h^*(\omega)G^*_{2D}(\mathbf{x}',\mathbf{x}_B,\omega)G_{2D}(\mathbf{x}',\mathbf{x}_A,\omega)\right], \tag{4}$$

where $\mathbf{x}_A$ is an arbitrary observation point, $\mathbf{x}_B$ is the location of a source within the area S bounded by ∂S, $h(\omega)$ is the Fourier transform a signal emitted at $\mathbf{x}_B$, and G_{2D} is the 2-D acoustic Green's function (e.g. Boschi & Weemstra 2015), which Boschi *et al.* (2018) show to be

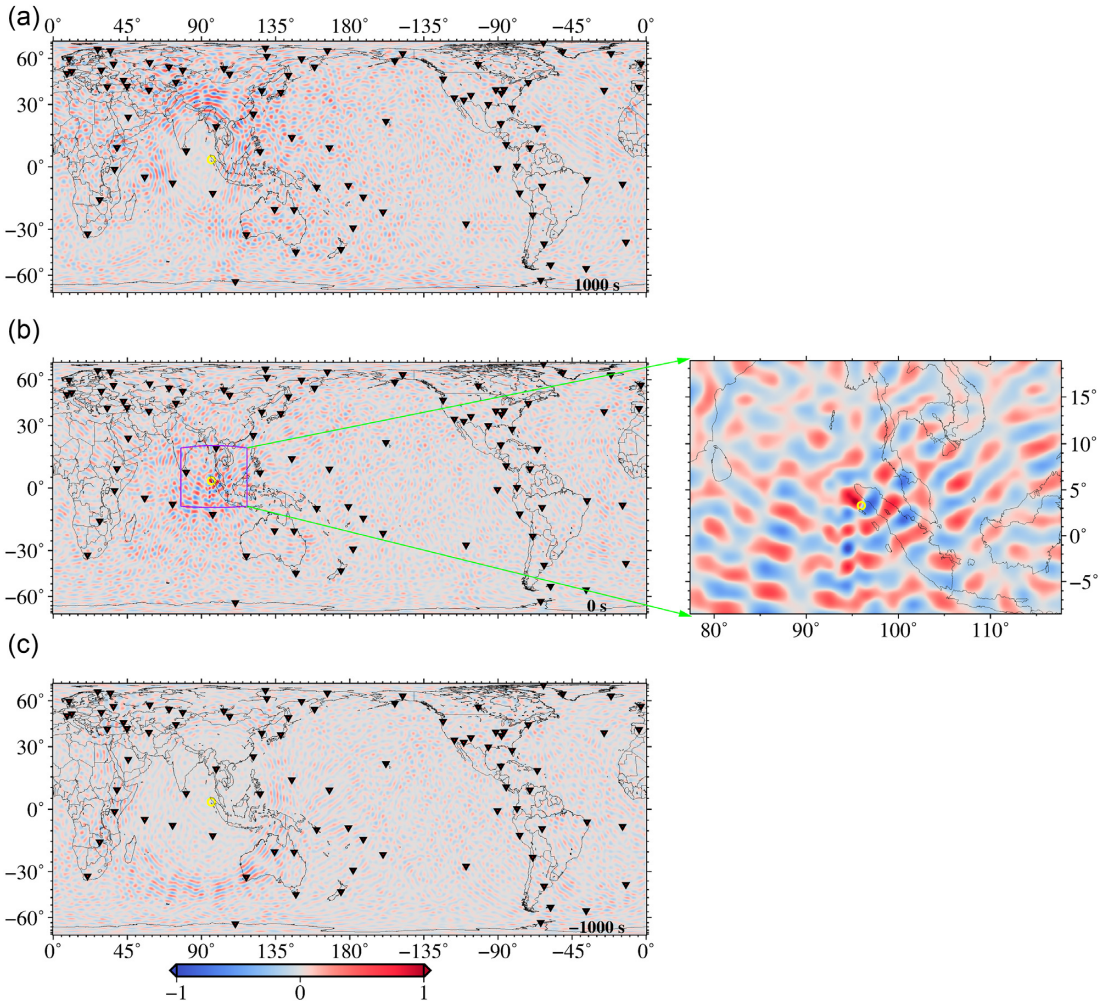

Figure 10. Snapshots of surface wave ray-tracing time reversal simulation of real earthquake (Sumatra earthquake, 2004 December 26, M_w 9.3), in the 80-to-120 s period band using recordings from 89 stations. We define $t = 0$ as earthquake origin time reported by the USGS. Snapshots (a) is taken at time $t = 1000$ s; (b) at $t = 0$ s and (c) at $t = -1000$s; negative t corresponds to time after focusing in a time-reversal simulation. The results were calculated in meters where as here and in the following, it is normalized so that the maximum of its absolute value for all mode-lled locations and times, is 1.

proportional to the vertical-component Rayleigh-wave Green's function. The left-hand side of eq. (4) can be simplified,

$$\left[G^*_{2D}(\mathbf{x}_A, \mathbf{x}_B, \omega) - G_{2D}(\mathbf{x}_A, \mathbf{x}_B, \omega)\right] h^*(\omega) = \{-2i\,\mathrm{Im}\,[G_{2D}(\mathbf{x}_A, \mathbf{x}_B, \omega)]\}\, h^*(\omega),$$

and it can be shown (e.g. appendix B of Boschi & Weemstra (2015) that

$$\mathrm{Im}(G_{2D}(\mathbf{x}_A, \mathbf{x}_B, \omega)) = -i\, G_o(\mathbf{x}_A, \mathbf{x}_B, \omega),$$

where $G_o(\mathbf{x_A}, \mathbf{x_B}, \omega)$ is a purely imaginary, odd function, whose inverse Fourier transform is:

$$G_o(\mathbf{x}_A, \mathbf{x}_B, t) = \frac{1}{2} G(\mathbf{x}_A, \mathbf{x}_B, t) - \frac{1}{2} G(\mathbf{x}_A, \mathbf{x}_B, -t).$$

It follows that the left-hand side of eq. (4) can be further rewritten

$$-2i\,\mathrm{Im}\,[G_o(\mathbf{x}_A, \mathbf{x}_B, \omega)]\, h^*(\omega) = +2i^2 G_o(\mathbf{x}_A, \mathbf{x}_B, \omega) h^*(\omega) = -2G_o(\mathbf{x}_A, \mathbf{x}_B, \omega) h^*(\omega).$$

Substituting into eq. (4), we obtain

$$h^*(\omega)\,[G_o(\mathbf{x}_A, \mathbf{x}_B, \omega)] \approx \frac{i\omega}{c_o} \int_{\partial s} d\mathbf{x}' [h^*(\omega) G^*_{2D}(\mathbf{x}', \mathbf{x}_B, \omega) G_{2D}(\mathbf{x}', \mathbf{x}_A, \omega)]. \tag{5}$$

Eq. (4) or (5) can be interpreted, for example, as follows. Look first at the right-hand side: the Rayleigh wave $h(\omega)$ emitted at $\mathbf{x}_B$ is recorded as $h(\omega)G_{2D}(\mathbf{x}', \mathbf{x}_B, \omega)$ at a set of points $\mathbf{x}'$ along a closed curve ∂S on the earth's surface; it is then time-reversed (hence the complex-conjugation

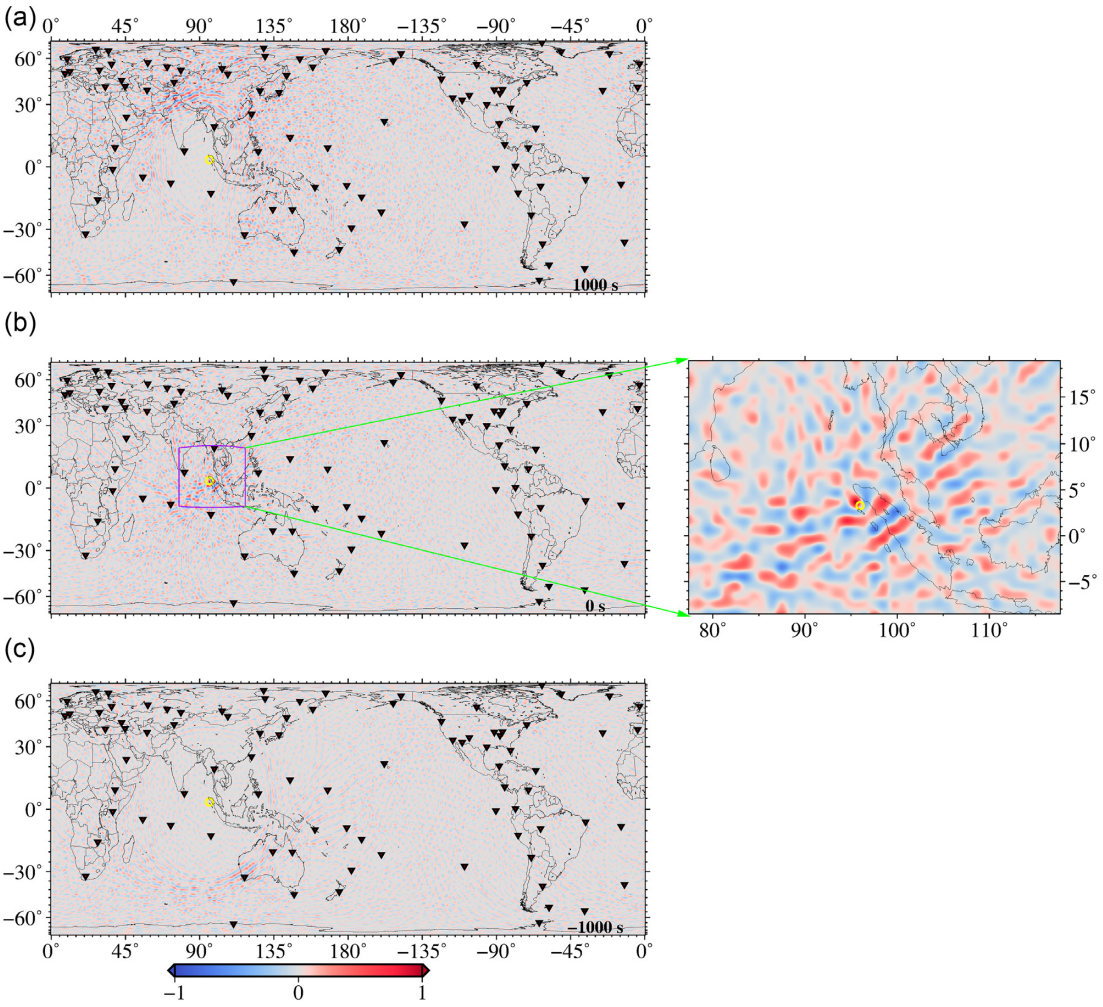

Figure 11. Snapshots of time-reversal simulations using earthquake data recorded by 89 stations, in the 50-to-110s period band. They are selected at the same time as in Fig. 10. All symbols are defined as in Fig. 10.

of $h(\omega)G_{2D}(\mathbf{x}', \mathbf{x}_B, \omega)$), re-emitted from $\mathbf{x}'$, and recorded at $\mathbf{x}_A$ (hence the convolution—multiplication in the frequency domain—with $G_{2D}(\mathbf{x}', \mathbf{x}_A, \omega)$). Now, integrating over ∂S is equivalent to having all receivers $\mathbf{x}'$ emitting their time-reversed recordings, whose sum is then received at $\mathbf{x}_A$. The result of all this, multiplied by $-\frac{i\omega}{c_o}$, must coincide with the product of $h^*(\omega)$ with $G_o(\mathbf{x}_A, \mathbf{x}_B, \omega)$. $h^*(\omega)$ is the Fourier transform of $h(-t)$, that is, the time-reversed version of the signal originally emitted at the source. Now, by the properties of Fourier transforms, the inverse Fourier transform of $h^*(\omega)G_o(\mathbf{x}_A, \mathbf{x}_B, \omega)$ coincides with the convolution of $h(-t)$ and $G_o(-t)$, that is,

$$F^{-1}\left[h^*(\omega)[G_o(\mathbf{x}_A, \mathbf{x}_B, \omega]\right] = \int_{-\infty}^{\infty} h(-\tau)G_o(\mathbf{x}_A, \mathbf{x}_B, t+\tau)d\tau. \tag{6}$$

Since the Green's function G_o is singular at zero distance from the source, we infer from eqs (5) and (6) that the time-reversed wavefield calculated according to their right-hand sides becomes singular for $\mathbf{x}_A = \mathbf{x}_B$, where in practice we expect to see a prominent maximum. In real-world applications, station distribution is often far from perfect, and not all azimuths can be covered with uniform density. This limits the accuracy with which the maximum of the time-reversed wavefield is correctly mapped at the source location $\mathbf{x}_B$.

For the sake of illustration, we implement the right-hand side of eq. (6), calculating the time-domain convolution of G_o [obtained by combining eqs (E15) and (B6) of Boschi & Weemstra (2015) and shown in Fig. 2b] with the source time function (100 s Ricker wavelet, Fig. 2a) used throughout this study. We take receiver $\mathbf{x}_A$ and source $\mathbf{x}_B$ to lay at a distance of 2000 km from one another, and constant wave speed $c = 4.12$ km s^{-1}. The resulting trace, shown in Fig. 2(c), is the time-reversed signal that would be modelled at $\mathbf{x}_A$, in an ideal time-reversal experiment, were stations re-emit from all azimuths.

Fig. 2(c) is a simplified illustration of the signal seen in time-reversal experiments: first, the time-reversed wavefield that eventually focuses at the source, and then, after focusing has occurred, a spurious arrival that is 'emitted' by the time-reversed source, and hits the receiver

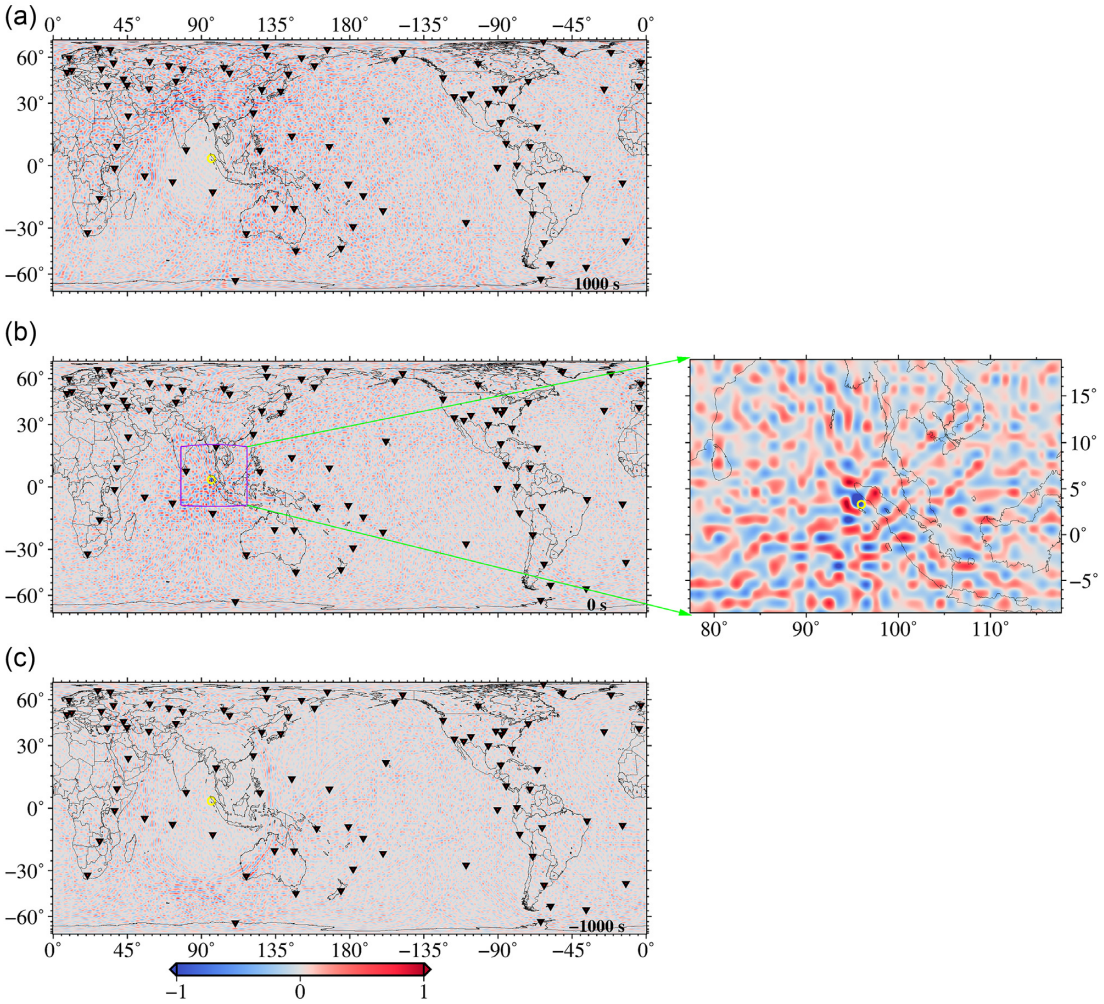

Figure 12. Snapshots of time-reversal simulations using earthquake data recorded by 89 stations, in the 40-to-90 s period band. They are selected at the same time as in Fig. 10. All symbols are defined as in Fig. 10.

again. This spurious signal is explained by the fact that the effectiveness of seismic and acoustic time reversal is limited by our inherent lack of knowledge of the source mechanism. Full time reversal of the seismic process would require that, in the reversed-time simulation, the source is replaced by an energy 'sink' which absorbs the signal, reversing the rupture process (slip along the fault) itself (Fink 2006): but such sink cannot be implemented if the slip is unknown.

3 COMPUTATIONAL COSTS

The computational cost of our method is driven by the number of source–receiver pairs and the choice of spatial separation between grid nodes; or, which is the same, the number of grid nodes. Simulations are quite demanding in terms of memory and computational runtime if performed on a single CPU. On the other hand, our scheme is easy to parallelize, as it consists of tracing rays between many source–receiver pairs, and each ray-tracing exercise is naturally independent of all the others.

In order to reduce the computational time, we run our time-reversal simulations on the 1664-CPUs ADA cluster at INGV, Bologna. We perform the entire time reversal simulation associated with one station on a single CPU, and run all one-station time reversals in parallel, so that, for 89 stations we used 89 CPUs. This way, the typical CPU time required to run one simulation, associated with one single frequency band, on the cluster is of the order of 10 hr. This coincides with the time required for full time reversal, as long as we have at least as many available CPUs as time-reversed seismograms (stations).

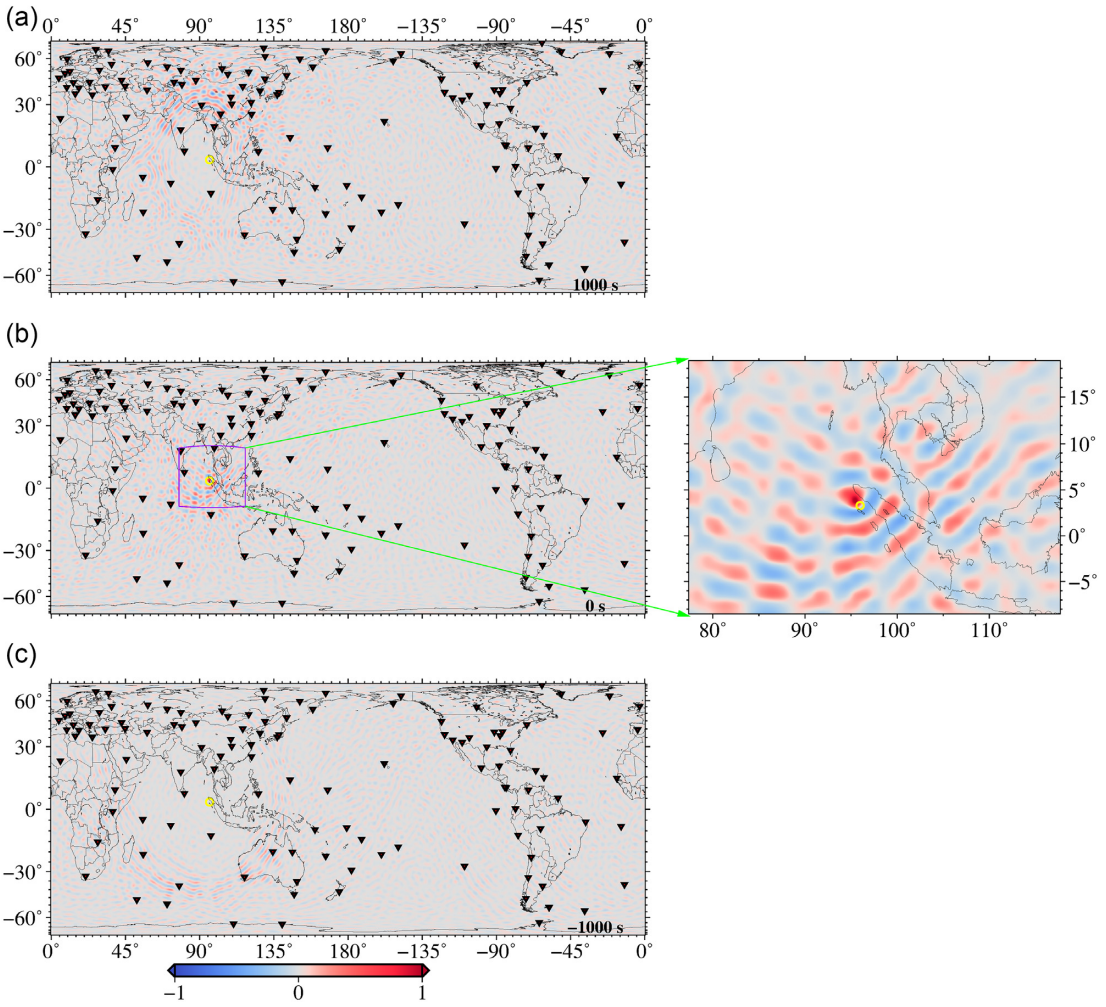

Figure 13. Snapshots of time-reversal simulations using earthquake data, in the 80-to-120s period band using 125 stations. All symbols are defined as in Fig. 10.

4 VALIDATION OF THE METHOD BY SYNTHETIC TESTS

We initially applied our method in a synthetic experiment using a 100 s Ricker wavelet as source time function. The globe is subdivided into an equal-area grid with $1^\circ \times 1^\circ$ spacing at the equator including 9834 grid nodes. Surface wave ray tracing is implemented as introduced in Section 2.1, after performing a least-square fitting via Cholesky factorization (Press *et al.* 1992) to find the generalized spherical-harmonic coefficients of the phase-velocity map. For any given virtual source (station) and receiver (grid node), we obtain traveltime and distance by tracing the ray between them. Then, we time reverse the recorded signals, and back propagate them with time by implementing eq. (5).

Synthetic data were first computed by propagating waves through the isotropic 100 s Rayleigh-wave phase-velocity map of Trampert & Woodhouse (2003). In the first test, stations were deployed along an equal-epicentral-distance curve (4500 km), equally spaced from one another. Fig. 3(d) shows that the time-reversed wavefield clearly focuses onto the 'input' source location; and, at the moment of focusing, no significant signal is seen away from the source.

In another test, we used synthetics from 89 selected station locations (II and IU networks), distributed as uniformly as possible over the globe. We show in Fig. 4 some snapshots of our time-reversal simulations. The reconstructed signal at the location of source is shown in Fig. 6 and the time-reversed wavefield focuses correctly at the expected location and origin time of the signal (Fig. 4b). In this case, however, the non-uniformity in station distribution results in significant non-zero time-reversed energy away (but not very far) from the source. Its pattern is determined by the interference between time-reversed wave fronts emitted by the different stations.

In order to test how the accuracy of the velocity model is important for the convergence of the method, we performed another test where we time-reversed and backpropagated the same synthetics as above, in a model that involved no lateral heterogeneity, that is, 100 s Rayleigh-wave phase velocity is constant and equal to 4 km s^{-1}. The time-reversed wavefield in Fig. 5 focuses at the location 247 km away

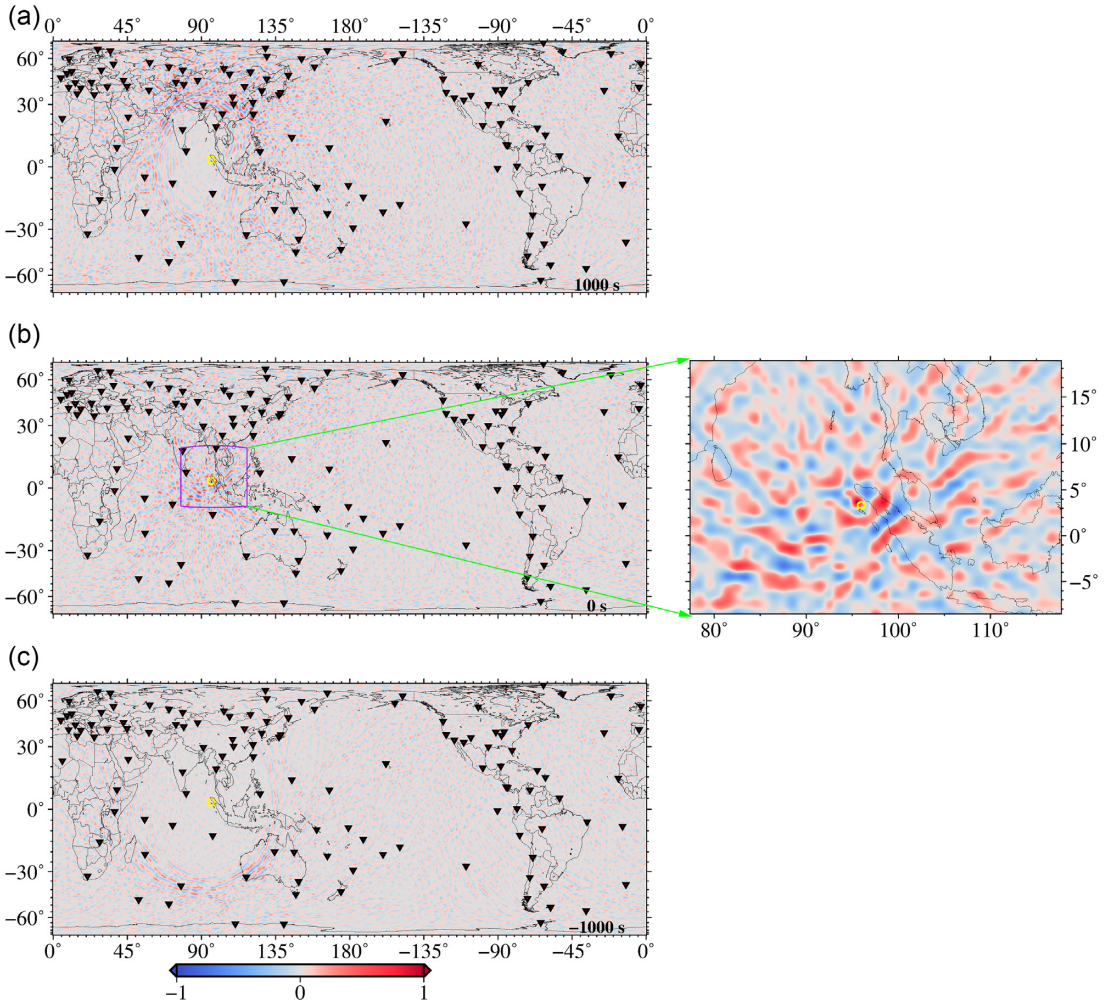

Figure 14. Snapshots of time-reversal simulations using earthquake data, in the 50-to-110 s period band using 125 stations. All symbols are defined as in Fig. 10.

from the correct source location. Fig. 5(e) shows the difference between the two cases: with and without the velocity model, that is, Figs 4(b) and 5(b). The main peak during the focusing is not as sharp as when a realistic, heterogeneous phase velocity model is used to backpropagate the synthetics as shown in Fig. 6.

A set of synthetic data was next computed based on Trampert & Woodhouse (2003) azimuthally anisotropic map of 100 s Rayleigh-wave velocity, neglecting the 4ζ term in eq. (1), and keeping the 2ζ and isotropic terms only. Fig. 7 shows some snapshots of our simulation. This new set of synthetics was then time-reversed and backpropagated twice: first in the same, anisotropic model used to compute them, and then in the isotropic model used earlier. The time-reversed wavefields so obtained are very similar, and differences in the mapped source area are minor. 'Anisotropic' time reversal of synthetics that contain anisotropy results in an excellent fit of the trace recorded at the source with the source time function while 'isotropic' time reversal of the same synthetic results in a 1 s error in focusing time (Fig. 8), but an essentially equivalent spatial distribution of the time-reversed signal as shown in Fig. 7. Thus, in the following, for the sake of simplicity, we only account for isotropic velocity heterogeneity in all our simulations.

5 APPLICATION TO EARTHQUAKE DATA

We apply our surface wave ray-tracing and time-reversal algorithm to recordings of the 2004 December 26, Sumatra–Andaman Earthquake, $M_w = 9.3$, 00:58:53. Being one of the largest and most studied earthquakes of all times, we use it as an ideal test case for our method because of its large energy release and to compare our results with those obtained from other techniques.

First, 89 seismograms were downloaded from the IRIS/USGS Global Seismographic Network (GSN, Fig. 10, black triangle) (Albuquerque Seismological Laboratory(ASL)/USGS, 1988; Scripps Institution of Oceanography, 1986), which we selected because of the relative spatial

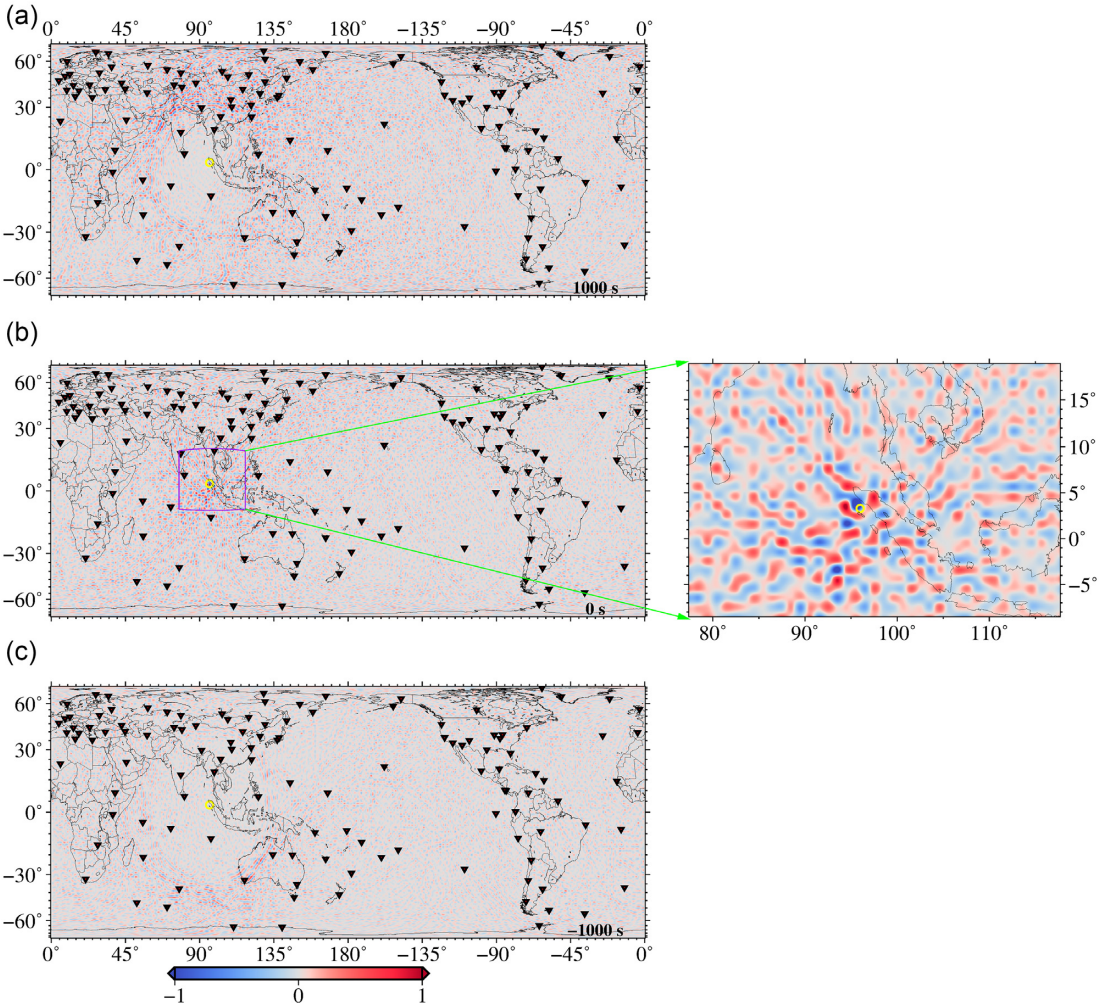

Figure 15. Snapshots of time-reversal simulations using earthquake data, in the 40-to-90 s period band using 125 stations. All symbols are defined as in Fig. 10.

uniformity in station distribution. Next, we further increased the number of stations from 89 to 125, including data from IC (ASL/USGS, 1992), MN (MedNet Project Partner Institutions, 1990) and G (GEOSCOPE, 1982) networks (Fig. 13). This way we verified whether our result varies with station coverage.

We remove the instrumental response for each trace, and apply a 80-to-120 s bandpass filter. Filtered data are shown in Fig. 9. We next apply the procedure described in Section 4. The heterogeneous phase velocity model for Rayleigh waves at 100 s is taken from Trampert & Woodhouse (2003). We find that the backward propagating wavefield focuses on the expected source location. We show in Fig. 10 snapshots of time-reversed wavefield. Fig. 10(b) shows the maximum focusing at 3.31°N and 95.85°E this corresponds to the USGS estimate of 3.316°N and 95.854°E. We repeat surface wave ray-tracing and time reversal simulation in the 40-to-90 and 50-to-110 s bands and show the results in Figs 11 and 12. Again, phase velocity maps at 60 and 80 s are taken from Trampert & Woodhouse (2003). The accuracy of source localization appears to be slightly decreased with a significant reduction in the width of the passband. Further, we increase the number of stations to 125 and then perform the time-reversal simulation for all those three bands. The results are consistent with those of the 89-station simulations as shown in Figs 13, 14 and 15 for 80-to-120, 40-to-90 and 50-to-110 s respectively, with sharpest focusing at the epicentre achieved in the respective band.

We next squared the time-reversed trace (80-to-120 s), then integrate it over time to obtain a proxy for the energy propagating through gridpoint j at time t,

$$E_j(t) = \frac{1}{t}\int_0^t a_j^2(t)dt \tag{7}$$

where $a_j(t)$ is the amplitude of the time-reversed signal at grid node j and time t. Because the signal a_j is a displacement, it is understood that E_j is not strictly energy. Still, its distribution in time and space should be very closely related to that of energy, at least at the scale length

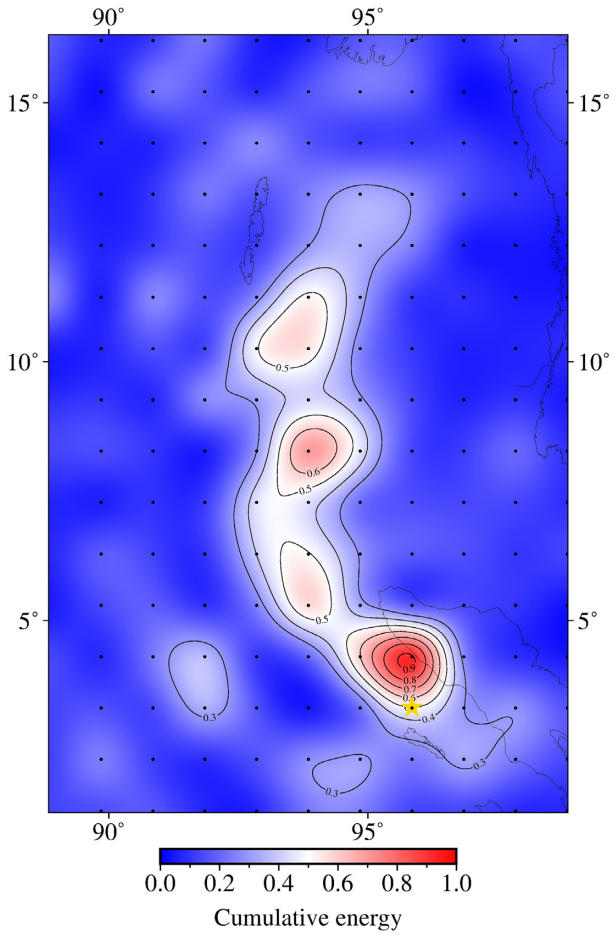

Figure 16. Proxy $E_j(t)$ for seismic energy defined by eq. (7) with $t = 600$ s, computed from data bandpass filtered between 80 and 120 s (as in Fig. 10). E_j is normalized to 1 and plotted only in the area where it is large, coinciding with the source region of the Sumatra event. The epicenter is denoted by a yellow star. The black contours are plotted at increments of 0.1.

that is of interest here. We therefore integrate $a_j^2(t)$ over 600 s after the initiation of the earthquake (Fig. 16) to obtain a rough estimate of the relative strength of total energy released as a function of location. We show in Fig. 17 how $E_j(t)$ varies with t over the grid and observe the migration of rupture from south towards the north with rupture lasting nearly 600 s after initiation of the earthquake. The plotted area is limited to the only part of the globe where an important amount of energy accumulates. Time in Fig. 17 is measured after initiation of the earthquake. We found the strongest energy radiation in the southern portion, to the west of the northern Sumatra, followed by a second important radiation to the north of the Nicobar Island, as depicted in Fig. 16.

Finally, we apply the same procedure of time-reversal in the 40-to-90 and 50-to-110 s passbands. The results are shown in Fig. 18. We average the energy radiation estimates obtained from the time reversal simulation at 40-to-90, 50-to-110 and 80-to-120 s passbands, and show it in Fig. 19. This confirms our earlier result, with large energy emission in two regions. In summary, our result are in good agreement with the conclusion drawn by Ishii *et al.* (2005, fig. 4), Krüger & Ohrnberger (2005, fig. 3) and Larmat *et al.* (2006) about the slip distribution and the migration of rupture in an unilateral direction from south towards the north.

6 SUMMARY AND CONCLUSIONS

We treat narrow-frequency band surface wave signals as membrane waves, which we model via ray tracing on the sphere similar to Boschi & Woodhouse (2006), thus reducing the computational weight of numerical simulations. Our surface wave ray-tracing algorithm is based on the generalized spherical harmonic parametrization, and the time reversal method is used to reconstruct the surface wavefield in the immediate vicinity of the source region. As an example, the spatial distribution of energy radiation from the 2004 Sumatra earthquake is estimated via our method. By comparison with independent studies based on different data and techniques, we infer that our method is successful in mapping the source of the earthquake in both space and time, tracing its direction of rupture propagation and locating areas where most energy

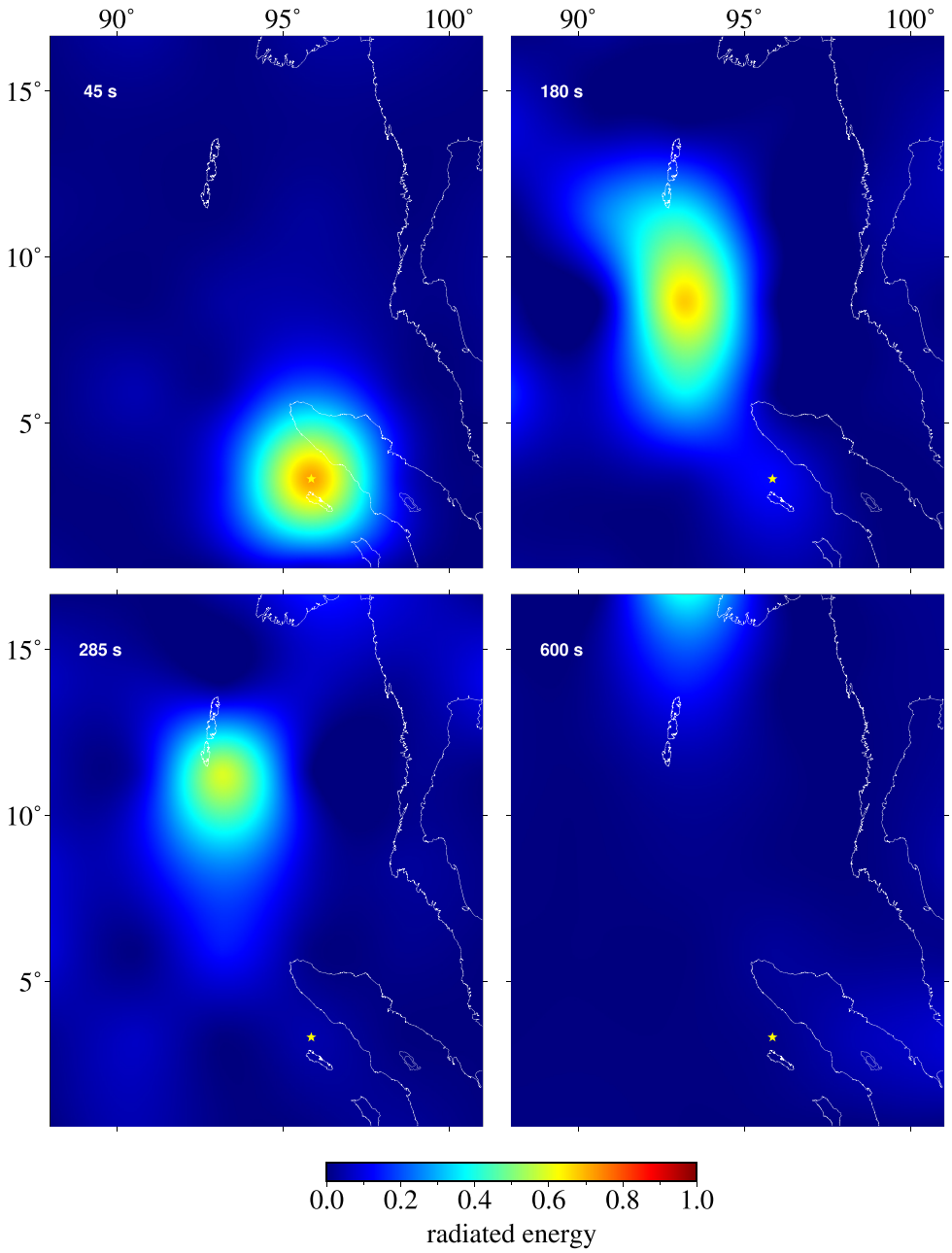

Figure 17. Rupture progression. The distribution of energy radiation at different time intervals. The rupture starts just west of northern Sumatra and advances in a northward direction all the way to Andaman Islands.

is released. Specifically, our results are in good agreement with existing finite-source models of the events (Ammon *et al.* 2005; Krüger & Ohrnberger 2005; Ni *et al.* 2005; Banerjee *et al.* 2005; Bletery *et al.* 2016). In all those models, most energy release occurs to the northwest of the Sumatra Island and near the Nicobar Island.

This study encourages further application of our method, in particular to the 3-D mapping of seismic faults, both in space and time. This will require the calculation of time reversal at a dense suite of surface wave modes, and their combination, with account of respective depth sensitivities. It will be the topic of future work. As discussed in many other studies (e.g. Fink 2006; Boschi *et al.* 2018), the time-reversed wavefield includes a non-physical contribution, that is, a signal that propagates away from the source after focusing, cannot be easily removed. For this non-physical effect to disappear, the source process itself should be modelled, introducing a time-reversed forcing term referred to as 'sink'. This issue will be addressed in future work.

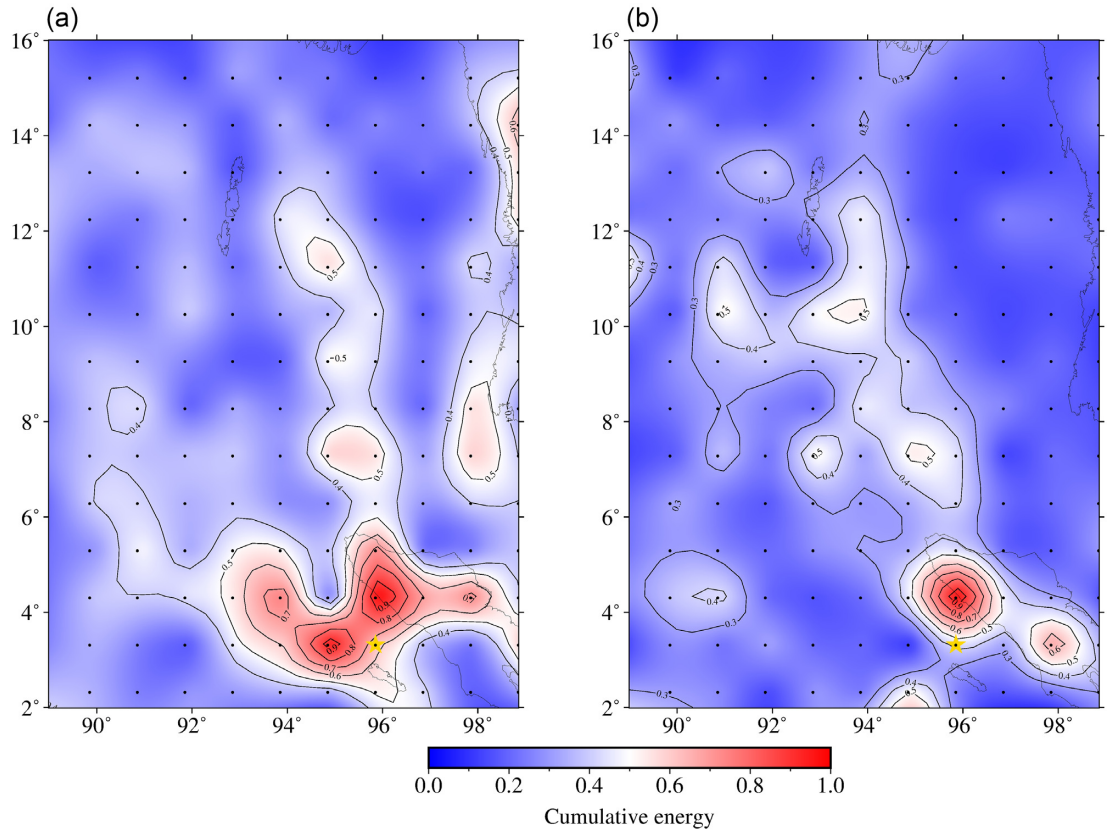

Figure 18. Integrated energy over 600 s after initiation of the earthquake obtained time-reversing seismograms bandpass filtered between (a) 40-to-90 s and (b) 50-to-110 s.

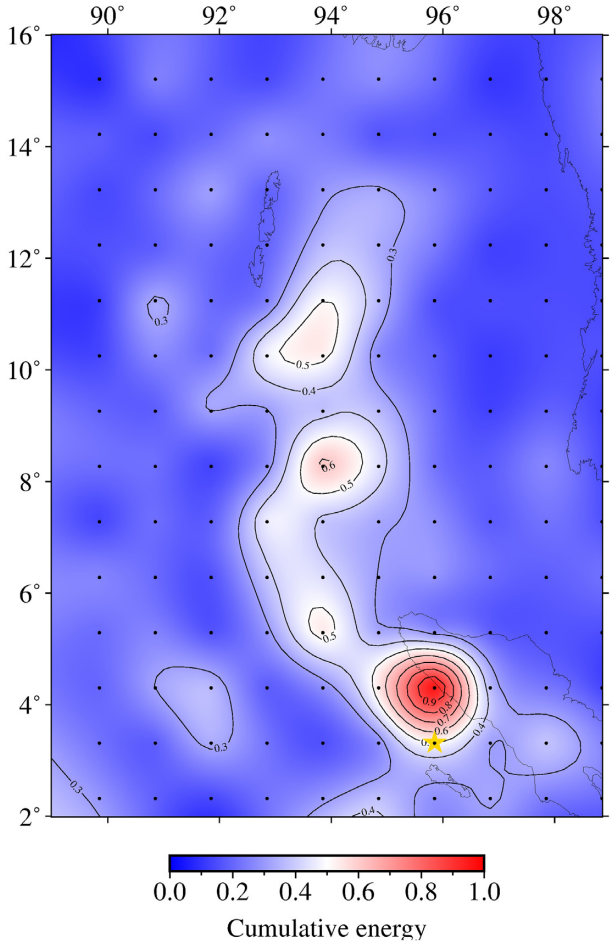

Figure 19. Cumulative energy radiation obtained by averaging results from time reversal in all three passbands.

ACKNOWLEDGEMENTS

We are grateful to Laura Ermert and Carène Larmat for their careful reviews, and to the editor, Eiichi Fukuyama.

DATA AVAILABILITY

The data that support the findings of this study were downloaded from all broad-band stations with channel name BHZ that are made publicly available through The IRIS Data Management Center (IRISDMC, http://service.iris.edu/fdsnws/dataselect/1/), including the following seismic networks: (1) IU (GSN; Albuquerque, 1988); (2) II [GSN; Scripps Institution of Oceanography (SIO), 1988]; (3) MN [Istituto Nazionale di Geofisica e Vulcanologia (INGV), 1988]; (4) IC [Albuquerque Seismological Laboratory (ASL)/USGS, 1992] and (5) G (Institut de Physique du Globe de Paris, 1982). All the plots in this paper were generated with the GMT (Wessel *et al.* 2013) and python toolboxes.

REFERENCES

Albuquerque Seismological Laboratory(ASL)/USGS, 1988. Global Seismograph Network (GSN-IRIS/USGS), *International Federation of Digital Seismograph Networks,* Other/Seismic Network, doi:10.7914/SN/IU.

Ammon, C.J. *et al.*, 2005. Rupture process of the 2004 sumatra-andaman earthquake, *Science,* **308**(5725), 1133–1139.

ASL/USGS, 1992. New China Digital Seismograph Network, *International Federation of Digital Seismograph Networks,* Other/Seismic Network, doi:10.7914/SN/IC.

Banerjee, P., Pollitz, F.F. & Burgmann, R., 2005. The size and duration of the sumatra-andaman earthquake from far-field static offsets, *Science,* **308**(5729), 1769–1772.

Bletery, Q., Sladen, A., Jiang, J. & Simons, M., 2016. A bayesian source model for the 2004 great sumatra-andaman earthquake, *J. geophys. Res.: Solid Earth,* **121**(7), 5116–5135.

Boschi, L., Molinari, I. & Reinwald, M., 2018. A simple method for earthquake location by surface-wave time reversal, *Geophys. J. Int.,* **215**(1), 1–21.

Boschi, L. & Weemstra, C., 2015. Stationary-phase integrals in the cross correlation of ambient noise, *Rev. Geophys.,* **53**(2), 411–451.

Boschi, L. & Woodhouse, J.H., 2006. Surface wave ray tracing and azimuthal anisotropy: a generalized spherical harmonic approach, *Geophys. J. Int.,* **164**(3), 569–578.

Catherine, J.K., Gahalaut, V.K. & Sahu, V.K., 2005. Constraints on rupture of the december 26, 2004, sumatra earthquake from far-field gps observations, *Earth planet. Sci. Lett.,* **237**(3-4), 673–679.

Ekström, G., Tromp, J. & Larson, E.W., 1997. Measurements and global models of surface wave propagation, *J. geophys. Res.: Solid Earth,* **102**(B4), 8137–8157.

Fink, M., 1999. Time-reversed acoustics, *Sci. Am.,* **281**(5), 91–97.

Fink, M., 2006. Time-reversal acoustics in complex environments, *Geophysics,* **71**(4), SI151–SI164.

Fink, M., Montaldo, G. & Tanter, M., 2003. Time-reversal acoustics in biomedical engineering, *Annu. Rev. Biomed. Eng.,* **5**(1), 465–497.

GEOSCOPE, 1982. French global network of broad band seismic stations, *Institut de physique du globe de Paris (IPGP), Université de Paris,* doi:10.18715/GEOSCOPE.G.

Guilbert, J., Vergoz, J., Schisselé, E., Roueff, A. & Cansi, Y., 2005. Use of hydroacoustic and seismic arrays to observe rupture propagation and source extent of the mw= 9.0 sumatra earthquake, *Geophys. Res. Lett.,* **32**(15), doi:10.1029/2005GL022966.

Hashimoto, M., Choosakul, N., Hashizume, M., Takemoto, S., Takiguchi, H., Fukuda, Y. & Fujimori, K., 2006. Crustal deformations associated with the great sumatra-andaman earthquake deduced from continuous gps observation, *Earth Planets Space,* **58**(2), 127–139.

Ishii, M., Shearer, P.M., Houston, H. & Vidale, J.E., 2005. Extent, duration and speed of the 2004 sumatra–andaman earthquake imaged by the hi-net array, *Nature,* **435**(7044), 933–936.

Jaffe, B.E. *et al.*, 2006. Northwest sumatra and offshore islands field survey after the december 2004 indian ocean tsunami, *Earthq. Spectra,* **22**(3_suppl), 105–135.

Krüger, F. & Ohrnberger, M., 2005. Tracking the rupture of the mw= 9.3 sumatra earthquake over 1,150 km at teleseismic distance, *Nature,* **435**(7044), 937–939.

Larmat, C., Montagner, J.-P., Fink, M., Capdeville, Y., Tourin, A. & Clévédé, E., 2006. Time-reversal imaging of seismic sources and application to the great sumatra earthquake, *Geophys. Res. Lett.,* **33**(19).

Larmat, C., Tromp, J., Liu, Q. & Montagner, J.-P., 2008. Time reversal location of glacial earthquakes, *J. geophys. Res.: Solid Earth,* **113**(B9), doi:10.1029/2008JB005607.

Larson, E.W., Tromp, J. & Ekström, G., 1998. Effects of slight anisotropy on surface waves, *Geophys. J. Int.,* **132**(3), 654–666.

Lay, T. *et al.*, 2005. The great sumatra-andaman earthquake of 26 december 2004, *Science,* **308**(5725), 1127–1133.

Lomax, A., 2005. Rapid estimation of rupture extent for large earthquakes: application to the 2004, m9 sumatra-andaman mega-thrust, *Geophys. Res. Lett.,* **32**(10), doi:10.1029/2005GL022437.

Mai, P.M. *et al.*, 2016. The earthquake-source inversion validation (siv) project, *Seismol. Res. Lett.,* **87**(3), 690–708.

MedNet Project Partner Institutions,1990. Mediterranean Very Broadband Seismographic Network (MedNet), *Istituto Nazionale di Geofisica e Vulcanologia (INGV),* doi:10.13127/SD/FBBBTDTD6Q.

Merrifield, M. *et al.*, 2005. Tide gauge observations of the indian ocean tsunami, december 26, 2004, *Geophys. Res. Lett.,* **32**(9), doi:10.1029/2005GL022610.

Ni, S., Kanamori, H. & Helmberger, D., 2005. Energy radiation from the sumatra earthquake, *Nature,* **434**(7033), 582–582.

Peter, D., Boschi, L. & Woodhouse, J., 2009. Tomographic resolution of ray and finite-frequency methods: a membrane-wave investigation, *Geophys. J. Int.,* **177**(2), 624–638.

Peter, D., Tape, C., Boschi, L. & Woodhouse, J.H., 2007. Surface wave tomography: global membrane waves and adjoint methods, *Geophys. J. Int.,* **171**(3), 1098–1117.

Press, W.H., Vetterling, W.T., Teukolsky, S.A. & Flannery, B.P., 1992. *Numerical Recipes Example Book (FORTRAN),* Cambridge University Press, Cambridge.

Rietbrock, A. & Scherbaum, F., 1994. Acoustic imaging of earthquake sources from the chalfant valley, 1986, aftershock series, *Geophys. J. Int.,* **119**(1), 260–268.

Roten, D., Miyake, H. & Koketsu, K., 2012. A Rayleigh wave back-projection method applied to the 2011 tohoku earthquake, *Geophys. Res. Lett.,* **39**(2), doi:10.1029/2005GL022610.

Scripps Institution of Oceanography, 1986. IRIS/IDA seismic network. *International Federation of Digital Seismograph Networks,* Other/Seismic Network, doi:10.7914/SN/II.

Smith, M.L. & Dahlen, F., 1973. The azimuthal dependence of love and rayleigh wave propagation in a slightly anisotropic medium, *J. geophys. Res.,* **78**(17), 3321–3333.

Smith, M.L. & Dahlen, F., 1975. Correction [to "'the azimuthal dependence of love and rayleigh wave propagation in a slightly anisotropic medium'by martin l. smith and fa dahlen"]', *J. geophys. Res.,* **80**(14), 1923–1923.

Tanimoto, T., 1990. Modelling curved surface wave paths: membrane surface wave synthetics, *Geophys. J. Int.,* **102**(1), 89–100.

Tanimoto, T. & Anderson, D.L., 1985. Lateral heterogeneity and azimuthal anisotropy of the upper mantle: Love and rayleigh waves 100–250 s, *J. geophys. Res.: Solid Earth,* **90**(B2), 1842–1858.

Trampert, J. & Woodhouse, J.H., 2003. Global anisotropic phase velocity maps for fundamental mode surface waves between 40 and 150 s, *Geophys. J. Int.,* **154**(1), 154–165.

Tromp, J. & Dahlen, F., 1993. Variational principles for surface wave propagation on a laterally heterogeneous earth—III. potential representation, *Geophys. J. Int.,* **112**(2), 195–209.

Vigny, C. *et al.*, 2005. Insight into the 2004 sumatra–andaman earthquake from gps measurements in southeast asia, *Nature,* **436**(7048), 201–206.

Wessel, P., Smith, W.H.F., Scharroo, R., Luis, J. & F., Wobbe, 2013. GMT 5: A major new release of the Generic Mapping Tools, in *Eos, Transactions of the American Geophysical Union,* Vol. **94,** pp. 409–410, doi:10.1002/2013EO450001.

Yao, H., Gerstoft, P., Shearer, P.M. & Mecklenbräuker, C., 2011. Compressive sensing of the tohoku-oki mw 9.0 earthquake: frequency-dependent rupture modes, *Geophys. Res. Lett.,* **38**(20), doi:10.1029/2011GL049223.